

Molecular clouds photoevaporation and FIR line emission

L. Vallini^{1,2,3*}, A. Ferrara^{4,5}, A. Pallottini^{4,6,7}, S. Gallerani⁴

¹*Nordita, KTH Royal Institute of Technology and Stockholm University, Roslagstullsbacken 23, SE-10691 Stockholm, Sweden*

²*Dipartimento di Fisica e Astronomia, viale Bertoni Pichat 6, I-40127 Bologna, Italy*

³*INAF, Osservatorio Astronomico di Bologna, via Ranzani 1, I-40127 Bologna, Italy*

⁴*Scuola Normale Superiore, Piazza dei Cavalieri 7, I-56126, Pisa, Italy*

⁵*Kavli IPMU (WPI), Todai Institutes for Advanced Study, the University of Tokyo, Japan*

⁶*Kavli Institute for Cosmology, University of Cambridge, Madingley Road, Cambridge CB3 0HA, UK*

⁷*Cavendish Laboratory, University of Cambridge, 19 J. J. Thomson Ave., Cambridge CB3 0HE, UK*

ABSTRACT

With the aim of improving predictions on far infrared (FIR) line emission from Giant Molecular Clouds (GMC), we study the effects of photoevaporation (PE) produced by external far-ultraviolet (FUV) and ionizing (extreme-ultraviolet, EUV) radiation on GMC structure. We consider three different GMCs with mass in the range $M_{\text{GMC}} = 10^{3-6} M_{\odot}$. Our model includes: (i) an observationally-based inhomogeneous GMC density field, and (ii) its time evolution during the PE process. In the fiducial case ($M_{\text{GMC}} \approx 10^5 M_{\odot}$), the photoevaporation time (t_{pe}) increases from 1 Myr to 30 Myr for gas metallicity $Z = 0.05 - 1 Z_{\odot}$, respectively. Next, we compute the time-dependent luminosity of key FIR lines tracing the neutral and ionized gas layers of the GMCs, ([C II] at $158 \mu\text{m}$, [O III] at $88 \mu\text{m}$) as a function of G_0 , and Z until complete photoevaporation at t_{pe} . We find that the specific [C II] luminosity is almost independent on the GMC model within the survival time of the cloud. Stronger FUV fluxes produce higher [C II] and [O III] luminosities, however lasting for progressively shorter times. At $Z = Z_{\odot}$ the [C II] emission is maximized ($L_{\text{CII}} \approx 10^4 L_{\odot}$ for the fiducial model) for $t < 1$ Myr and $\log G_0 \geq 3$. Noticeably, and consistently with the recent detection by Inoue et al. (2016) of a galaxy at redshift $z \approx 7.2$, for $Z \leq 0.2 Z_{\odot}$ the [O III] line might outshine [C II] emission by up to ≈ 1000 times. We conclude that the [O III] line is a key diagnostic of low metallicity ISM, especially in galaxies with very young stellar populations.

Key words: ISM: clouds - infrared: ISM - galaxies: ISM - line: formation - galaxies: high-redshift

1 INTRODUCTION

Giant molecular clouds (GMCs) are the reservoirs of molecular gas fuelling the star formation (SF) in galaxies. The complex network of physical processes linking the SF with the global evolution of a GMC it is often referred to as *feedback* (see McKee & Ostriker 2007, and references therein). Feedback determines the rate at which GMCs eventually return their gas to the diffuse phase of the interstellar medium (ISM), hence setting the efficiency of the subsequent episodes of star formation which thus are self-regulated. The feedback processes acting on GMCs scales are ultimately due to radiative and/or mechanical energy injection, both within and from outside the clouds.

External momentum, can be provided by supernova (SN) explosions and superbubbles (e.g. Wada & Norman

2001; Elmegreen & Scalo 2004), and by spiral shocks (Bonnell et al. 2006). Internally, the mechanical energy is provided by jet/outflows/winds from protostars and newly formed stars (e.g. Norman & Silk 1980; Dale et al. 2013; Nakamura & Li 2014), SN explosions (e.g. Walch & Naab 2015; Kim et al. 2016; Körtgen et al. 2016), and expanding H II regions powered by newborn star clusters within the cloud (e.g. Bertoldi 1989; Williams & McKee 1997; Krumholz et al. 2006; Vázquez-Semadeni et al. 2010; Dale et al. 2014). More precisely the ionizing photons produced by young massive stars forming into (or close by) GMCs produce H II regions that, by expanding into the ambient gas, energize the molecular clouds, thus contributing to the large-scale turbulent power (Elmegreen & Scalo 2004, and references therein). Supersonic turbulence inhibits the collapse of GMCs and regulate the SF efficiency (Mac Low & Klessen 2004; Vázquez-Semadeni et al. 2005; Krumholz & McKee 2005; Padoan et al. 2014). In spite of this, the

* E-mail: livia.vallini@su.se

net effect of star formation is negative, and ultimately photoevaporates and unbinds GMCs in a few dynamical times (Bertoldi 1989; Bertoldi & McKee 1990; Gorti & Hollenbach 2002; Krumholz et al. 2006).

Beside extreme UV (EUV), ionizing ($h\nu < 13.6\text{ eV}$) photons, also far-ultraviolet (FUV) photons ($6\text{ eV} < h\nu < 13.6\text{ eV}$) strongly affect the chemistry, thermal balance, structure, and dynamics of GMCs. FUV radiation dissociates molecular gas beyond the H II region, creating photodissociation regions (PDRs, Hollenbach & Tielens 1999) from which most infrared (IR) emission of galaxies originates. Dust grains and polycyclic aromatic hydrocarbons, absorb radiation from the stars and reradiate this energy in the IR; at the same time photoelectrons heat the gas (Wolfire et al. 2003). Radiative cooling is enabled by many far infrared (FIR) lines. The importance of FIR line emission in constraining the ISM properties (e.g. gas temperature, density, and metallicity) has driven the advances in the IR and sub-millimeter astronomy. Nowadays, with the Atacama Large Millimeter/Submillimeter Array (ALMA) we can aim at constraining the properties of PDRs and those of the associated molecular clouds in the first galaxies. One of the ALMA primary goals is the detection of the (redshifted) [C II] from the high- z Universe (e.g. Carilli & Walter 2013) even though the physical interpretation of the line measurement from high redshift is often very challenging (Maiolino et al. 2015; Gallerani et al. 2016; Knudsen et al. 2016). Many recent efforts (Nagamine et al. 2006; Vallini et al. 2013, 2015; Olsen et al. 2015; Pallottini et al. 2015, 2017; Gallerani et al. 2016) have been devoted to relate the physical properties of neutral and molecular gas in high- z galaxies to the FIR line luminosity. However, radiative feedback effects have not yet been included in such relation. Here we aim at making this step.

Our plan is to model the time evolution of FIR line emission from a single GMC illuminated by nearby massive stars. Our investigation builds upon previous studies (Bertoldi 1989; Bertoldi & McKee 1990; Gorti & Hollenbach 2002) on GMC photoevaporation (PE) induced by externally-produced EUV/FUV photons impinging on the cloud. We adopt their analytic formalism to model the PE process and compute the time-evolution of the GMC density field. Then, by coupling the model with the photoionization/photodissociation code CLOUDY, we self-consistently calculate the evolving luminosity of several FIR lines. Among these, the [C II] $158\mu\text{m}$ fine structure line is often the most luminous and it is considered the work-horse for high- z galaxy exploration. We focus our attention also on [O III] at $88\mu\text{m}$, originating from the outer, ionized shell. The final goal is to assess whether (and how) PE, by affecting the density field of the GMCs, modulates FIR line emission under a range of different metallicity and irradiation conditions.

The paper is structured as follows: in Section 2 we describe how we model (i) the internal structure of the GMCs, and (ii) the radiation field impinging on the clouds. Then, we treat the photoevaporation theory in Sec. 3 presenting the model results. In Section 4 we show how the evolving density field in GMCs impacts FIR line emission. We draw our conclusions in Section 5, where also some caveats are discussed.

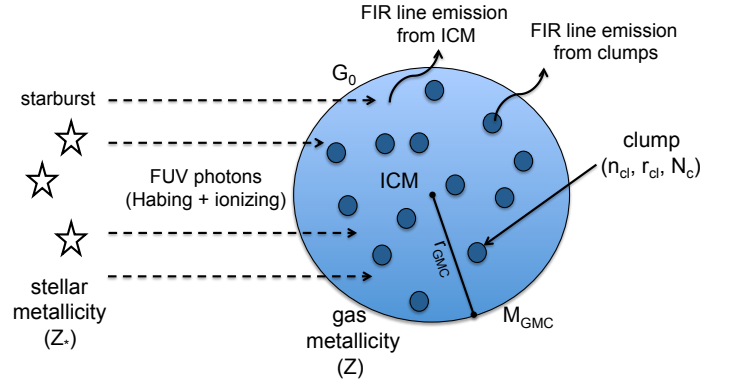


Figure 1. Sketch of the GMC model used in this work.

2 MODEL

A schematic description of our model is shown in Fig. 1. We consider an idealized case of a clumpy, starless GMC immersed in an external radiation field. The effects of gas clumpiness on the PDR structure and the resulting FIR line emission have been studied also by Meixner & Tielens (1993). Those calculations, however, do not account for time evolution of the density field and feedback effects. The key features entering our model are: (i) the GMC density structure, and (ii) the radiation field. These are discussed in detail in the following Sections.

2.1 GMC density structure

Molecular clouds are observed to have a hierarchical structure with a density field showing enhancements (usually referred to as clumps and filaments) on $\approx 0.1 - 10$ pc scales. The typical hydrogen column density of a GMC is $N_H \approx 10^{22}\text{ cm}^{-2}$ (e.g. McKee & Ostriker 2007, and references therein) but variations are observed in the range $N_H \approx 10^{21} - 10^{23}\text{ cm}^{-2}$. GMCs are supported against collapse by turbulence and magnetic fields.

Numerical and analytical studies conclude that the Probability Distribution Function (PDF) of the gas density, ρ , in a supersonically turbulent, isothermal cloud of mean density ρ_0 is lognormal:

$$g_s ds = \frac{1}{(2\pi\sigma_s^2)^{1/2}} \exp\left[-\frac{1}{2}\left(\frac{s-s_0}{\sigma_s}\right)^2\right] \quad (1)$$

with $s \equiv \ln(\rho/\rho_0)$ (e.g. Vazquez-Semadeni 1994; Krumholz & McKee 2005; Padoan & Nordlund 2011; Hennebelle & Chabrier 2011, 2013; Kim et al. 2003; Wada 2008; Tasker & Tan 2009; Federrath & Klessen 2013). The mean logarithmic density (s_0) is related to the standard deviation of the distribution (σ_s) by $s_0 = -\sigma_s^2/2$ which, in turn, depends on the sonic Mach number (\mathcal{M}), and the ratio of thermal to magnetic pressure (β) as:

$$\sigma_s^2 = \ln\left(1 + b^2 \mathcal{M}^2 \frac{\beta}{\beta + 1}\right). \quad (2)$$

The b factor in the previous equation parametrizes the kinetic energy injection mechanism (often referred to as forcing) driving the turbulence ($b \approx 0.3 - 1$, see Molina et al. 2012, for an extensive discussion).

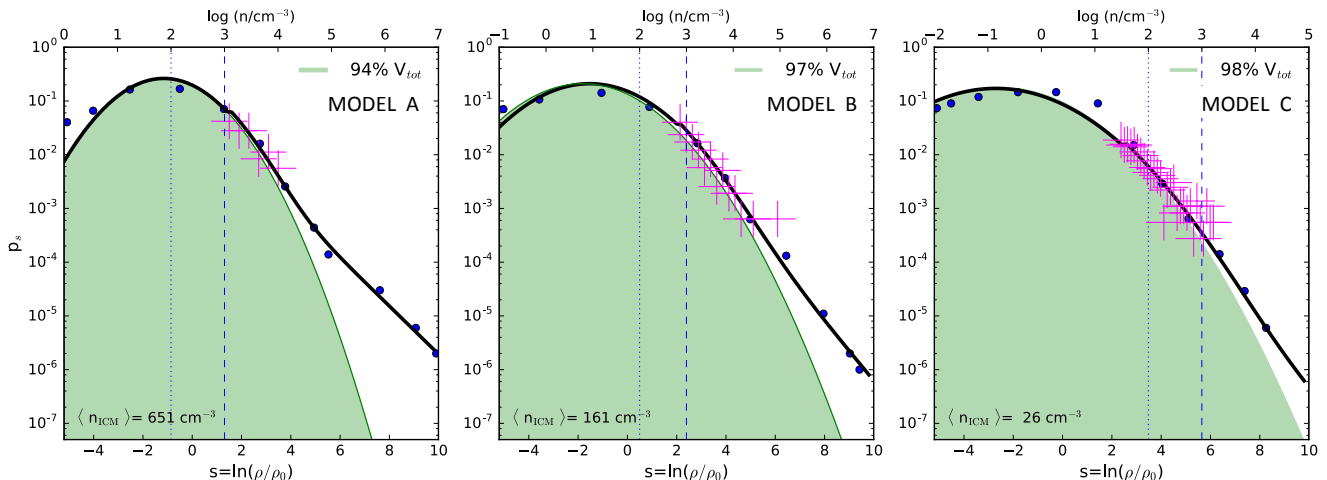


Figure 2. Volume-weighted PDFs (blue points) of the logarithmic density $s \equiv \ln(\rho/\rho_0)$ simulated by Federrath & Klessen (2013) for GMCs models A, B, C in Table 1. The solid black line is the best lognormal + power-law fit to the numerical results. The volume fraction filled by the log-normally distributed gas (green area) is given for each model. The upper x -axis provides the gas number density n , along with the reference values $n = 10^2, 10^3 \text{ cm}^{-3}$. Magenta crosses show the density of sampled GMC clumps (see Sec. 2.1 for details on the procedure adopted).

Table 1. Properties of the GMC models considered in this work

model	$M_{\text{GMC}} [M_{\odot}]$	$r_{\text{GMC}} [\text{pc}]$	\mathcal{M}	$\rho_0 [\text{g cm}^{-3}]$
A	6.2×10^3	4	10	8.2×10^{-22}
B	9.9×10^4	16	20	2.1×10^{-22}
C	3.9×10^6	100	50	3.3×10^{-23}

When self-gravity is included, the PDF develops a power-law tail ($p_s \propto \rho^{-\kappa}$) at high densities. The occurrence of the power-law tail is confirmed both theoretically (e.g. Krumholz & McKee 2005; Hennebelle & Chabrier 2011; Padoan & Nordlund 2011; Federrath & Klessen 2013), and observationally via dust extinction measurements (e.g. Kainulainen et al. 2009; Lombardi et al. 2015; Stutz & Kainulainen 2015; Schneider et al. 2015) or molecular line detections (e.g. Goldsmith et al. 2008; Goodman et al. 2009; Schneider et al. 2015) carried out in nearby GMCs. While dust extinction allows to probe a larger dynamic range (a measured visual extinction $A_V = 1 - 100 \text{ mag}$ corresponds to clump column densities (N_{cl}) in the range $N_{cl} \approx 10^{21} - 10^{23} \text{ cm}^{-2}$), molecular line detections are limited to the high density tail of the PDF ($N_{cl} > 10^{23} \text{ cm}^{-2}$). Here we consider three different cloud models (named A, B, and C, with properties summarized in Tab. 1) in order to bracket the range of values observed in Galactic GMCs, and those assumed in simulations by Federrath & Klessen (2013)

We set up the internal density of the clouds so that their PDFs are in agreement with that found by Federrath & Klessen (2013) for $\mathcal{M} = 10, 20, 50$, mean gas density $\rho_0 = 8.2 \times 10^{-22}, 2.1 \times 10^{-22}, 3.3 \times 10^{-23} \text{ g cm}^{-3}$, and turbulence forcing parameter $b \approx 0.3$. In Fig. 2, we show the PDF that has been fitted with a lognormal (g_s , eq. 1) function + power-law (t_s) tail, i.e. $p_s = g_s + t_s$. In what follows, we identify two components in the GMC, referred to as *clumps* and diffuse *interclump medium* (ICM), adopting a criterion based on the density PDF. We use the term *clumps* to de-

note small scale structures ($< 1 \text{ pc}$ in size) that are part of the power-law tail. In the literature, clumps have been interpreted either as temporary density fluctuations produced by supersonic turbulence (Falgaronne & Phillips 1990), or as stable physical entities confined by ICM pressure (Williams et al. 1995). Even though clump morphology is observed to vary from filamentary to quasi-spherical shapes, in our work we model the clumps as spheres (see Fig. 1).

The volume filled by the gravitationally unstable clumps in the GMCs is:

$$V_{clumps} = V_{\text{GMC}} - V_{\text{ICM}} \quad (3)$$

where the volume of the ICM is given by the log-normal distribution

$$V_{\text{ICM}} = V_{\text{GMC}} \int g_s ds. \quad (4)$$

We obtain $\int g_s ds = 0.94, 0.97, 0.98$ for models A, B, and C, respectively (see Fig. 2). To build the internal density field we then use the following procedure:

1. Randomly extract from the tail t_s the i -th clump with number density¹ $n_{cl,i} = \rho/(\mu m_p)$.
2. Calculate the clump radius as the turbulent Jeans length:

$$r_{cl,i} = \frac{1}{2} \lambda_{J,turb} = \frac{1}{2} \frac{\pi \sigma^2 + \sqrt{36\pi c_s^2 GL^2 \rho + \pi^2 \sigma^4}}{6GL\rho} \quad (5)$$

where c_s is the sound speed. Eq. 5 is obtained by using an effective (turbulent+thermal) pressure term in the Jeans length equation (see eqs. 35, 36 in Federrath & Klessen 2012).

3. Calculate the clump volume $V_{cl,i} = (4/3)\pi r_{cl,i}^3$.

¹ We assume the gas to be a mixture of hydrogen and helium with mean molecular weight $\mu = 1.22$.

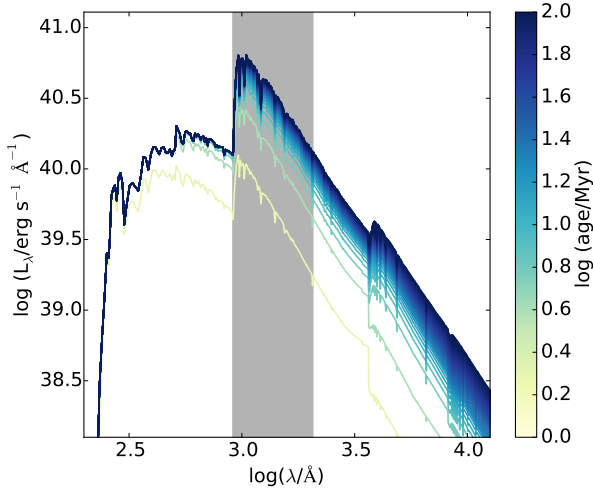


Figure 3. Spectral energy distribution (SED) of the radiation field produced by stars with $Z_* = 0.2 Z_\odot$ as a function of time elapsed from the onset of the star formation. We assume a continuous SFR of $1 M_\odot \text{ yr}^{-1}$. The gray shaded region highlights the Habing band.

4. Iterate steps 1-3 until $\sum_i V_{cl,i} = V_{clumps}$.

Finally, we compute the total mass in clumps $M_{tot,cl} = \sum_i \frac{4}{3} \pi \mu m_p n_{cl,i} r_{cl,i}^3$, the ICM total mass $M_{ICM} = M_{GMC} - M_{tot,cl}$, and the ICM mean density $\langle n_{ICM} \rangle = M_{ICM} / (\mu m_p V_{ICM})$. The resulting clump distributions are shown with magenta crosses in Fig. 2. For model A, B and C we find $M_{tot,cl} \approx 1.2 \times 10^3, 1.8 \times 10^4, 7.2 \times 10^5 M_\odot$, and $\langle n_{ICM} \rangle \approx 651, 161, 26 \text{ cm}^{-3}$, respectively.

2.2 Radiation field

The spectral energy distribution (SED) of the radiation field impinging on the GMC surface is calculated using the stellar population synthesis code *Starburst99* (Leitherer et al. 1999), assuming a Salpeter Initial Mass Function in the range $1 - 100 M_\odot$. We adopt the Geneva standard evolutionary tracks (Schaller et al. 1992) with metallicity $Z_* = 1 Z_\odot, 0.2 Z_\odot$, and $0.05 Z_\odot$, and Lejeune-Schmutz stellar atmospheres which incorporate plane-parallel atmospheres and stars with strong winds (Lejeune et al. 1997; Schmutz et al. 1992). We follow the time evolution of the SED between $1 - 100 \text{ Myr}$ considering a continuous star formation mode. The star formation rate is a free parameter of the model. As an example, we show the SED for $\text{SFR} = 1 M_\odot \text{ yr}^{-1}$ and $Z = 0.2 Z_\odot$ in Fig. 3. The lines are color-coded as a function of the starburst age. The gray shaded region highlights the non-ionizing FUV Habing band relevant to the PDR modeling; the strength of the FUV radiation is usually parameterized by G_0 , the ratio of the FUV flux to the one measured by Habing (1968) in the Milky Way ($\approx 1.6 \times 10^{-3} \text{ erg cm}^{-2} \text{ s}^{-1}$). As expected for a continuous star formation mode, the specific luminosity in the Habing

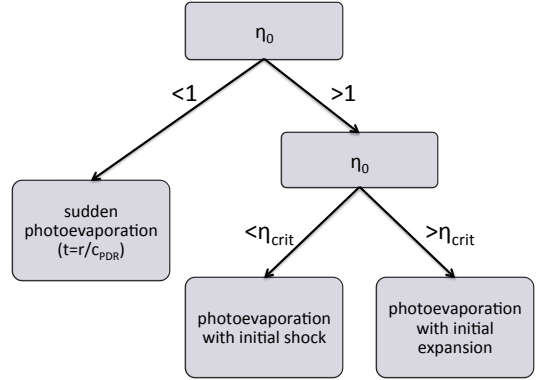


Figure 4. The three channels of the photoevaporation process. See text for the discussion of the various bifurcation parameters.

band increases with time before saturating to an asymptotic value around 100 Myr^2 .

3 PHOTOEVAPORATION

The UV radiation produced by massive OB stars influences the structure, dynamics, chemistry, and thermal balance of the surrounding gas. Ultraviolet photons substantially alter the clump-interclump structure of GMCs: EUV and/or FUV photons heat the surface layer of clumps to high temperatures causing the loss of their cold molecular mass that is ionized and/or photodissociated and it is converted into warm ionized/atomic gas (Hollenbach & Tielens 1999). This process is called *photoevaporation*. When the GMC is embedded in an HII region, the ICM is exposed to both EUV and FUV photons, while the internal clumps see only the attenuated FUV radiation. Penetration of EUV and FUV photons in the ICM and clumps is further addressed in Appendix A. There we show the temperature, x_{HI} , and G_0 profiles obtained with photoionization simulations discussed in detail in Sec. 3.2.

3.1 Analytical approach

Gorti & Hollenbach (2002) show that the evolution of a turbulent clump, impulsively irradiated by FUV photons is influenced only by two parameters: (a) the ratio of the clump initial column density ($n_{cl}^0 r_{cl}^0$) to the column (N_0) penetrated by the FUV radiation,

$$\eta_0 \equiv \frac{n_{cl}^0 r_{cl}^0}{N_0}, \quad (6)$$

² The SED can be approximated as a power-law of the form $\log L_\lambda = \alpha \log \lambda + \text{const}$ for $\lambda > 912 \text{ \AA}$. At the times relevant for photoevaporation, we find $\alpha = -2.2$ (age 1 Myr) and $\alpha = -2.4$ (age 10 Myr).

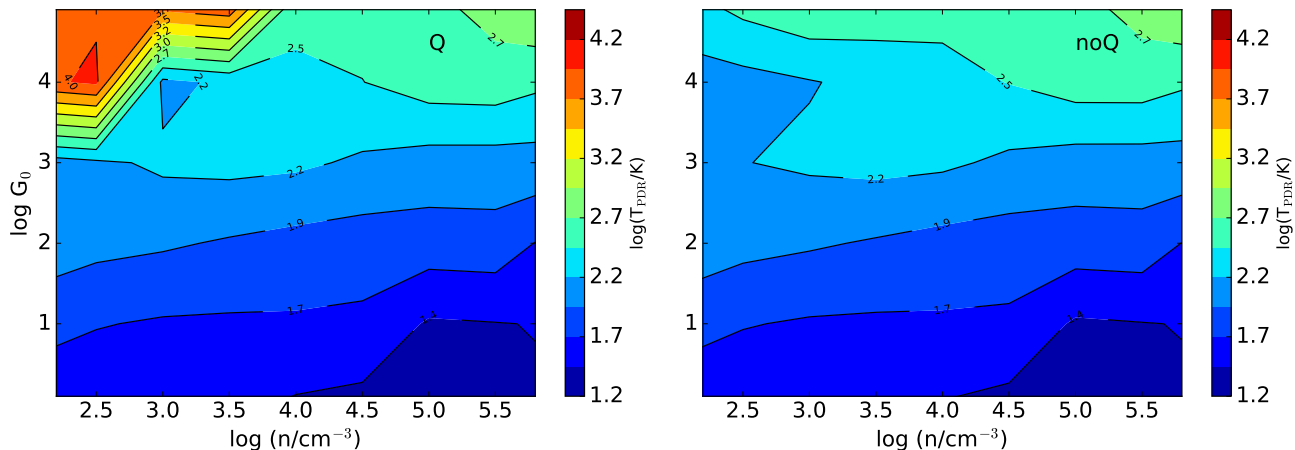


Figure 5. PDR temperature as a function of the gas density, n , and Habing flux, G_0 , for Q models (left) and noQ models (right) for a solar metallicity gas. T_{PDR} is measured where the FUV ($\lambda_{\text{ref}} = 1000\text{\AA}$) optical depth $\tau_{\text{FUV}} = 1$.

i.e. the depth into the cloud where $\tau_{\text{FUV}} \approx 1$; (b) the strength of the FUV field, parametrized by the ratio of the sound speed in the FUV-heated region (c_{PDR}) to the sound speed of the clump in the no-field case³:

$$\nu \equiv c_{\text{PDR}}/c_c. \quad (7)$$

If the ICM, as in the turbulent origin scenario previously discussed, has negligible pressure compared to the clumps, their evolution depends on the value of η_0 . Small clumps with $\eta_0 \leq 1$ are rapidly (on timescales of order of $t_c \approx r_{\text{cl}}/c_{\text{PDR}}$) heated and photodissociated by the FUV flux. Larger clumps ($\eta_0 > 1$) can confine the FUV-heated region to a thin surface layer. For large clumps, an additional bifurcation point exists (see the sketch in Fig. 4) at a critical value⁴ $\eta_{\text{crit}} \approx 4\nu^2/3$.

- If $\eta_0 < \eta_{\text{crit}}$ the FUV radiation produces a PDR shell whose pressure is initially much higher than that of the cold clump gas and a shock is driven into the clump, compressing it. N_{cl} remains roughly constant due to mass loss via photoevaporation; as a result the density increases during the compression phase. Once the shock has reached the center, the shrinking rate slows down, and it is purely regulated by mass loss from the surface.

- If $\eta_0 > \eta_{\text{crit}}$, the PDR shell is very thin compared to the clump size. The outer edge of the shell expands at roughly c_{PDR} , and its pressure drops rapidly. Hence, the clump pressure eventually becomes higher than the shell one triggering the expansion also of the clump gas (at the corresponding sound speed c_c). This expansion continues until pressure balance with the outer PDR layers is established. At this point the cold clump loses mass gradually, with an evolution similar to the final solution for shock-compressed clumps.

³ The parameter ν is therefore proportional to the square root of the ratio of the gas temperature in the PDR (T_{PDR}), over the initial temperature of the clump (T_c)

⁴ The critical value can be derived from mass conservation and from the condition of pressure equilibrium at the surface of the clump. For details see Gorti & Hollenbach (2002).

Gorti & Hollenbach (2002) derive analytical equations describing the time evolution of the density, radius and mass of the clumps in the two regimes. We refer the reader to Appendix B for details, and to Gorti & Hollenbach (2002) for a complete discussion.

3.2 Parameter evaluation

The parameters η_0 and ν depend on the PDR column density N_0 (see Eq. 6) and temperature T_{PDR} (see Eq. 7). In turn, these quantities depend on the clump density, n_{cl} , and G_0 :

$$N_0 = N_0(G_0, n_{\text{cl}}); \quad T_{\text{PDR}} = T_{\text{PDR}}(G_0, n_{\text{cl}}). \quad (8)$$

We calculate N_0 and T_{PDR} with version c13.03 of CLOUDY (Ferland et al. 2013), which allows us to model the transition between the H II region, PDR, and molecular part of a gas slab illuminated by a given radiation field. For each of the three metallicities⁵ considered in this work ($Z = 0.05, 0.2, 1 Z_{\odot}$) we run two sets of simulations with different prescriptions for the external radiation spectrum: (a) a full spectrum (Q models) including both FUV and EUV photons, (b) a FUV spectrum only (noQ models). The Q models (noQ models) are designed to mimic the flux reaching GMC placed within (outside) an H II region.

We run a total of 66×3 CLOUDY simulations for each metallicity, and for $\log(n/\text{cm}^{-3}) = [1 - 6]$ (in steps of 0.5 dex), and $\log G_0 = [0 - 5]$ (1 dex). The parameter space covers the plausible range of clumps/ICM densities (see Sec. 2.1), and Habing fluxes in galaxies. The code computes the radiative transfer through the slab up to a hydrogen column density $N_{\text{H}} = 10^{23} \text{cm}^{-2}$. This stopping criterium is chosen to (i) cover the whole range of column densities of our randomly generated clumps, and (ii) to fully sample the molecular part of the illuminated slab, typically located at $N_{\text{H}} \gtrsim 2 \times 10^{22} \text{cm}^{-2}$.

⁵ We do not make a distinction between gas and stellar metallicities, which are then supposed to be equal

We adopt the gas-phase abundances ($C/H = 3.0 \times 10^{-4}$, $O/H = 4.0 \times 10^{-4}$, $Mg/H = 3.0 \times 10^{-6}$, $N/H = 7.0 \times 10^{-5}$, $S/H = 1 \times 10^{-5}$) provided by CLOUDY for the Orion Nebula (Rubin et al. 1991; Osterbrock et al. 1992; Rubin et al. 1993)⁶, scaled with the metallicity of each specific model. The model accounts for the CMB background at $z = 6$, that can suppress the emergent line luminosity of FIR lines when observed in contrast with the CMB (Gong et al. 2012; da Cunha et al. 2013; Vallini et al. 2015; Pallottini et al. 2015; Zhang et al. 2016). In the calculation we consider a cosmic-ray (CR) ionisation rate $\zeta_{CR} = 2 \times 10^{-16} \text{s}^{-1}$ (Indriolo et al. 2007). Note, as a caveat, that the variation of the CR ionisation rate has strong effects on the chemistry and emission of PDRs (e.g. Papadopoulos et al. 2011; Bayet et al. 2011; Meijerink et al. 2011; Bisbas et al. 2015).⁷ The CRs, unlike FUV radiation, travel nearly unimpeded through the clouds and provide a source of input energy by: (i) freeing electrons, and (ii) inducing an internal UV field through the excitation of H_2 (see also Indriolo & McCall 2013, and references therein).

In Figure 5, we plot T_{PDR} as a function of the gas number density (n) and Habing flux (G_0) for $Z = Z_\odot$ where the FUV ($\lambda_{ref} = 1000\text{\AA}$) optical depth $\tau_{FUV} = 1$. This criterion is chosen because the temperature T_{PDR} entering in the Gorti & Hollenbach (2002) model (see Sec. 3), refers to the FUV-heated region, i.e. extending up to the point at which the FUV optical depth reaches a value of the order of unity.

The PDR temperatures obtained with `Q models` and `noQ models` are similar, apart from low-density ($n < 10^3 \text{cm}^{-3}$) and strong field ($G_0 > 10^3$) regimes, where `Q models` are warmer. The results are in agreement with those found by Kaufman et al. (1999) (see also Fig. 19 in Visser et al. 2012). Furthermore, as a sanity check, we compare T_{PDR} with that obtained by Bothwell et al. (2016) using the 3-D PDR code (Bisbas et al. 2012). Bothwell et al. (2016) cover the same range of G_0 and n considered here, but they sample the PDR temperature deeper into the gas slab ($A_V = 3$). As expected, our results ($T_{PDR} \approx 10^{1.2-2.5} \text{K}$, in the range $G_0 = [10^0 - 10^4]$ and $n = [10^2 - 10^5] \text{cm}^{-3}$) are slightly higher than those ($T_{PDR} \approx 10^{1.1-2.0} \text{K}$) found by Bothwell et al. (2016) (see their Fig. 10) in the same range of n and G_0 .

Once the PDR temperature and column density as a function of n and G_0 are known, we can determine the values of η_0 and ν for each cloud. This allows us to compute the time evolution of their mass, density and radius (see Appendix B). At each time step t_i , we update the value

⁶ As a caveat, we note that, in the standard CLOUDY set for the Orion Nebula, the carbon and oxygen abundances provided are ≈ 2 and ≈ 1.5 times greater than the values reported by e.g. Cardelli et al. (1996, $C/H = 1.4 \times 10^{-4}$) and Cartledge et al. (2004, $O/H = 2.8 \times 10^{-4}$), respectively.

⁷ The effect of the variation of ζ_{CR} on the $[C II]$ (CO) line intensity has been quantified by e.g. Meijerink et al. (2011) who show that for a PDR of density $n = 10^3 \text{cm}^{-3}$, irradiated by $G_0 = 10^3$, $I_{CII} = [4.4 - 8.6] \times 10^{-4} \text{ergs}^{-1} \text{sr}^{-1}$ ($I_{CO} = [7.6 - 0.28] \times 10^{-8} \text{ergs}^{-1} \text{sr}^{-1}$) when varying $\zeta_{CR} = 5 \times [10^{-17} - 10^{-14}] \text{s}^{-1}$. Recently Bisbas et al. (2015) have argued that CR-induced destruction of CO in GMCs is likely the single most important factor controlling the CO-visibility in star-forming galaxies.

of η_0 and ν according to the clump density at the previous time step, $n_{cl}(t_{i-1})$, assuming that G_0 is constant with time. (Bothwell et al. 2016; Visser et al. 2012)

3.3 Clump photoevaporation

Figs. 6 and 7 show the time evolution of the clump density and mass distribution for the three model clouds A, B, C. We concentrate on the effect G_0 variations on clumps photoevaporation at fixed metallicity, $Z = Z_\odot$. We define a clump as completely photoevaporated at time t , and hence removed from the clump inventory, if one of the two following conditions is satisfied: (i) the radius $r_{cl}(t) = 0$, or (ii) the clump density $n_{cl}(t) = \langle n_{ICM} \rangle$, i.e. the clumps become indistinguishable from the ICM. For $\log G_0 = 0$ the photoevaporation proceeds mainly via expansion. The density distribution shifts toward lower values. However, a small fraction ($< 1\%$ in mass, see Fig. 7) of longer-lived, compressed clumps is visible in the high density tail at $t = 10^6 \text{yr}$. On the contrary, for $\log G_0 = 2$, photoevaporation proceeds via shock compression for all the clumps, and the distribution shifts toward higher densities. These trends hold for both model A and B; model C is initially less dense (see Fig. 2) and the compression mode becomes important already for $\log G_0 = 0$.

During photoevaporation mass loss takes place, and a certain fraction of the clump mass is returned to the ICM. For $\log G_0 = 0$, such fraction after 10^4yr is $f_4 = 0.77 - 0.88$ depending on the cloud model; for $\log G_0 = 2$ mass loss is more substantial, $f_4 = 0.78 - 0.99$. We note that fixed G_0 at the clump surface, f_4 and f_6 (the analogous fraction after 1 Myr) increase going from model A, to B, to C, along their decreasing clump density sequence.

3.4 ICM photoevaporation

ICM photoevaporation is computed with a procedure similar to that adopted for the clumps. However, for the ICM the effects of EUV photons become important if the GMC is located within an H II region. For example, consider the case $\log G_0 \geq 5$ and $Z = Z_\odot$. Then, the typical column density of the H II layer in a gas of $n \approx 100 \text{cm}^{-3}$ is $N_{HII} \approx 10^{22} \text{cm}^{-2}$ (see Fig. A1, and the discussion in Appendix A), and thus comparable to the ICM column density. This implies that the GMC is almost fully ionized, and that photoevaporation is driven by the increased temperature ($T_{HII} \approx 10^4 \text{K}$) in the ionized layer.

To model this regime we adopt a modified version of the photoevaporation equations in Appendix B. In the equations for the time evolution of radius, mass, and density, we replace the parameter η_0 (see Eq. 6) with:

$$\eta_0^{\text{HII}} \equiv \frac{n_{\text{ICM}} r_{\text{GMC}}}{N_{\text{HII}}}, \quad (9)$$

where N_{HII} is the column density of the H II layer. Moreover, we substitute ν (see Eq. 7) with:

$$\nu^{\text{HII}} \equiv \frac{c_{\text{HII}}}{c_c} \quad (10)$$

where c_{HII} is the sound speed in the ionized layer. Note that $\nu_{\text{HII}} > \nu$, due to the higher temperature in the H II region with respect to PDRs. As in the case of clumps, η_0^{HII} and ν_{HII}

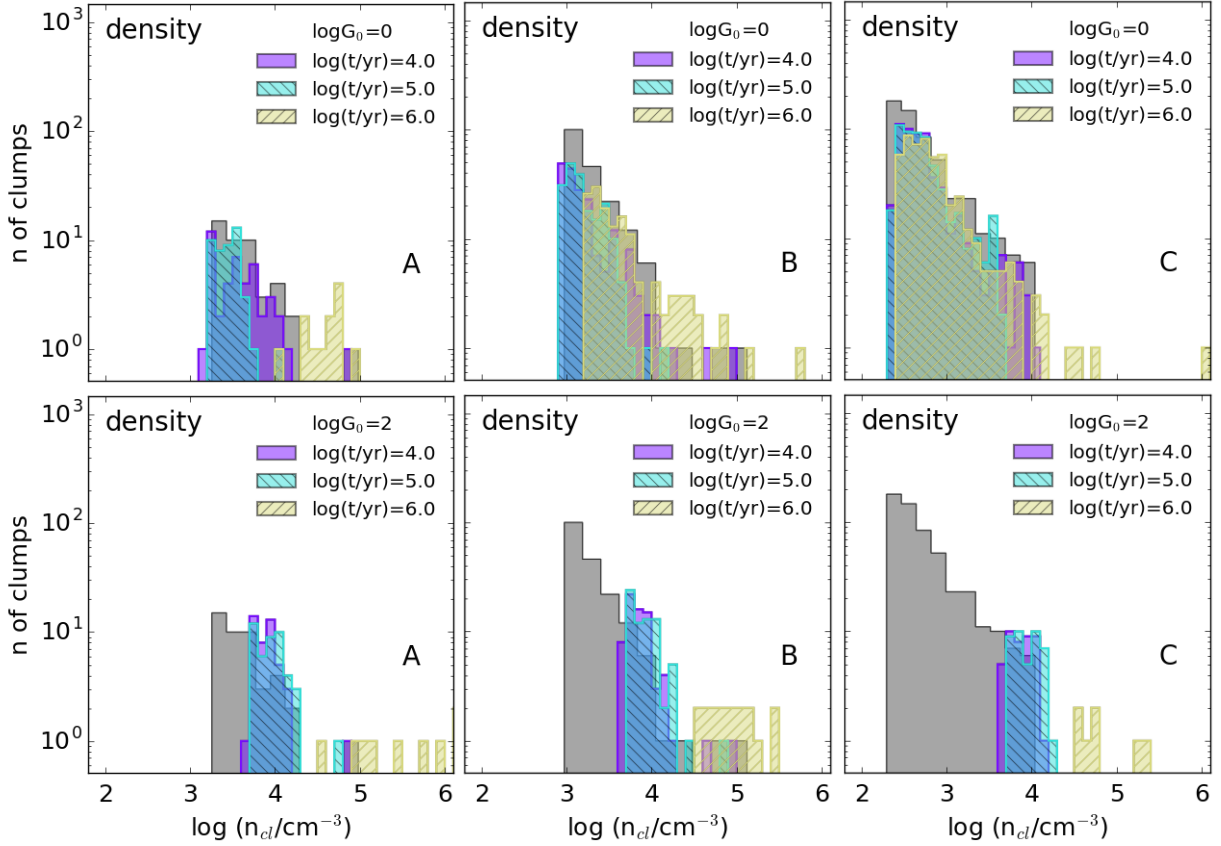


Figure 6. Time evolution of the clump density distributions for models A, B, C as a function of G_0 at the clump surfaces ($\log G_0 = 0, 2$, top and bottom row respectively). The distributions at $t = 10^4, 10^5, 10^6$ yr are shown with transparent colored histograms, and the initial distribution is shown in solid gray. Photoevaporated clumps are removed from the distribution.

depend on N_{HII} and T_{HII} , which have been determined from CLOUDY simulations at the depth at which the gas is 50% ionized. We follow the evolution of ICM density, GMC radius and mass until complete GMC photoevaporation, defined by one of the two criteria: (i) $M_{\text{ICM}} < 10\% M_{\text{GMC}}$, or (ii) the ICM density falls below $\approx 10 \text{ cm}^{-3}$, i.e. the typical density of the diffuse cold neutral ISM phase (Wolfire et al. 2003).

3.5 GMC photoevaporation timescales

In Fig. 8 we plot the GMC photoevaporation time (t_{pe}) as a function of G_0 for different metallicities, $Z = 1, 0.2, 0.05 Z_{\odot}$. At fixed cloud mass and G_0 , a decreasing Z results in a faster photoevaporation. This trend is mostly driven by the decreasing dust-to-gas ratio allowing the deeper UV radiation penetration to heat the internal gas layers. As a final remark we note that, for $Z = Z_{\odot}$ the maximum $t_{pe} \approx 30$ Myr in model B is consistent with the results by Williams & McKee (1997); Krumholz et al. (2006). These authors find $t_{pe} \approx 30 - 40$ Myr for GMCs of mass $10^5 M_{\odot}$ when considering the photoevaporation produced by OB associations inside the GMC.

4 FIR LINE EMISSION

From our model, we now compute the FIR line emission from GMCs, including the effects of PE. At each time step in the computation, we derive the line luminosity of the clumps (ICM) depending on their actual density, $n_{cl}(t)$ ($n_{\text{ICM}}(t)$), emitting area, $\pi r_{cl}(t)^2$ ($\pi r_{\text{GMC}}(t)^2$), and column density $N_{cl}(t) = n_{cl}(t)r_{cl}(t)$ ($N_{\text{ICM}}(t) = n_{\text{ICM}}(t)r_{\text{GMC}}(t)$). Again, we use CLOUDY to compute the FIR line flux, $I_{\text{line}}(n, G_0, N_{\text{H}})$ (in $\text{erg s}^{-1} \text{cm}^{-2}$), at the relevant surface (clump/ICM). The total luminosity is calculated as a sum over the clumps and the ICM:

$$L_{\text{line}}(t) = \sum_{cl} I_{\text{line}}(\langle f_{\text{att}} \rangle G_0, n_{cl}(t), N_{cl}(t)) \pi r_{cl}^2(t) + I_{\text{line}}(G_0, n_{\text{ICM}}(t), N_{\text{ICM}}(t)) \pi r_{\text{GMC}}^2(t). \quad (11)$$

In the above expression, the UV flux seen by the clumps is attenuated by the ICM by an average factor $\langle f_{\text{att}} \rangle = G_0(\langle N_{\text{H}} \rangle)/G_0$ to roughly account for GMC-scale radiative transfer effects not included here. The mean absorbing column density to each clump is $\langle N_{\text{H}} \rangle \approx 0.25 r_{\text{GMC}} n_{\text{ICM}}$. For models A, B, C, we get $\langle N_{\text{H}} \rangle \approx 2 \times 10^{21} \text{ cm}^{-2}$, yielding $\langle f_{\text{att}} \rangle \approx 0.2, 0.72, 0.9$ for $Z = 1, 0.2, 0.05 Z_{\odot}$. See App. A for further discussion on this point.

The predicted specific (i.e. per unit mass of emitting material) [C II] luminosity, ϵ_{CII} , is shown in Fig. 9 for the different cloud models. Such predictions are in very good agree-

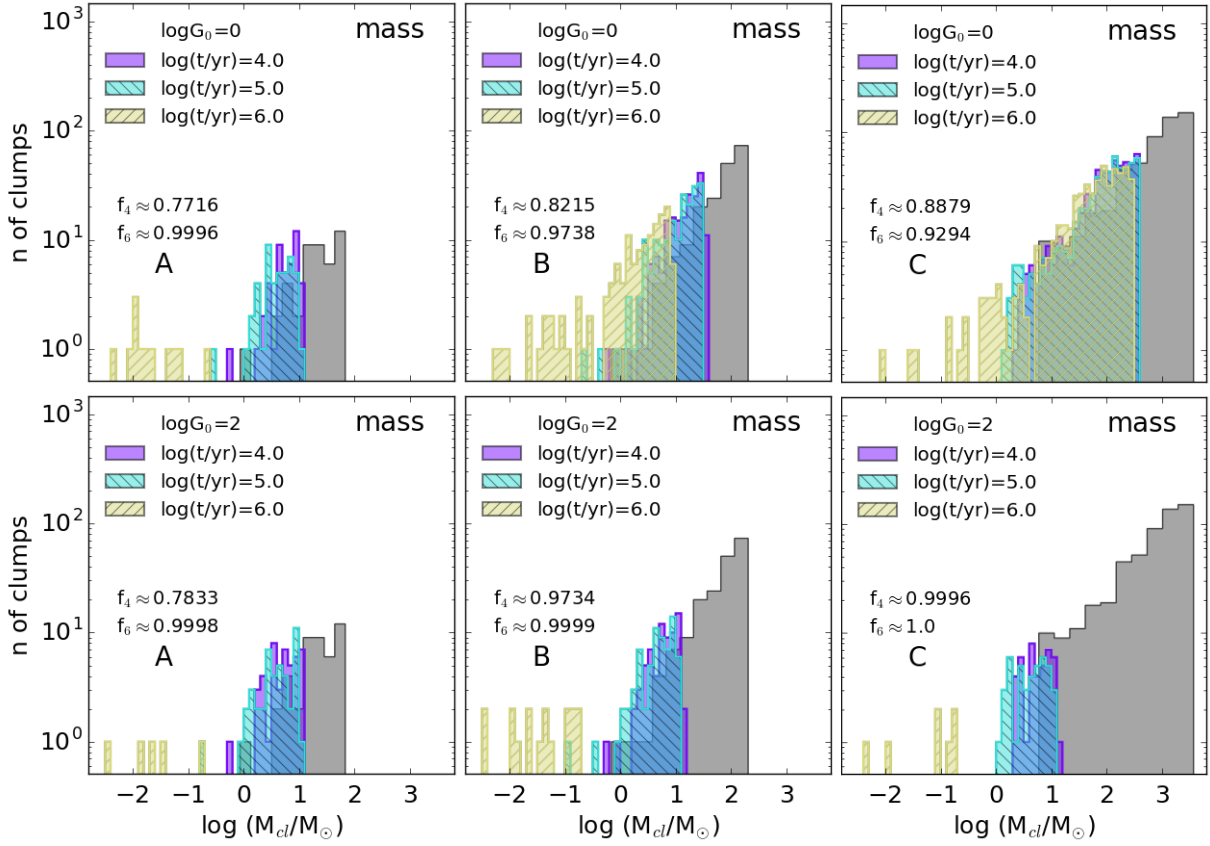


Figure 7. Same as Fig. 6 but for the clump mass distribution. The fraction of mass returned to the ICM at $t = 10^4, 10^6$ yr (f_4, f_6 , respectively) is given in each panel.

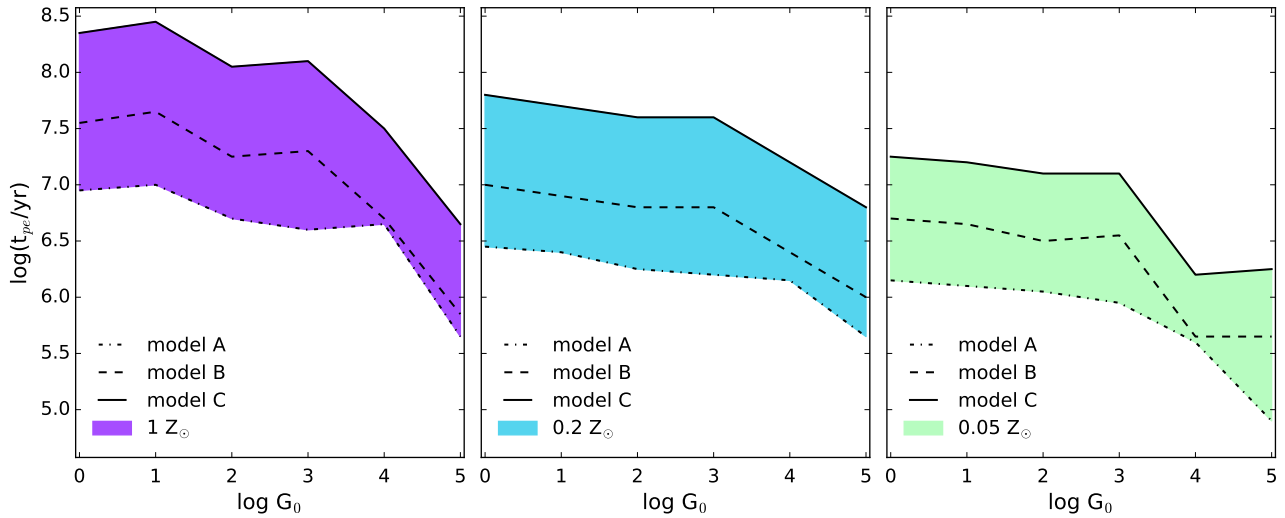


Figure 8. GMC photoevaporation time (t_{pe}) vs. G_0 for $Z = 1, 0.2, 0.05 Z_\odot$ from left to right). In each panel, the dashed line represents t_{pe} for our fiducial cloud (model B). The shaded area highlights the variation of t_{pe} for model C (solid lines) and model A (dot-dashed lines).

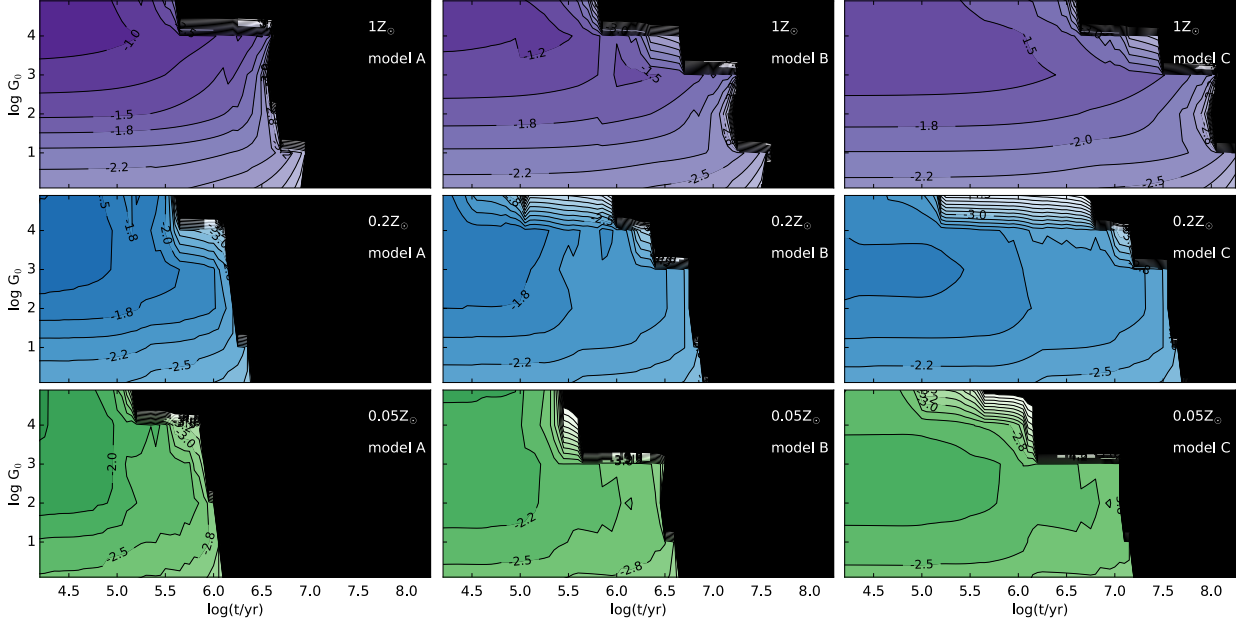


Figure 9. Specific [C II] luminosity (in units of L_{\odot}/M_{\odot}) evolution for cloud models A, B, C from left to right respectively as a function of G_0 and different metallicities ($Z = Z_{\odot}$ upper panels, $Z = 0.2 Z_{\odot}$ middle, and $Z = 0.05 Z_{\odot}$ bottom). Black regions denote $\epsilon_{\text{CII}} < 10^{-5}$.

ment with recent observations, e.g., of the Orion Molecular Cloud 1 (OMC1) by Goicoechea et al. (2015). The observed total mass in OMC1 region is $M_{\text{gas}} = 2600 M_{\odot}$, thus comparable with M_{GMC} in model A. Additionally, Goicoechea et al. (2015) measured a mean value of $G_0 \simeq 2 \times 10^4$, and a specific luminosity $L_{\text{CII}}/M_{\text{gas}} = 0.16 L_{\odot}/M_{\odot}$. This is consistent with our predictions for the same G_0 at $Z = Z_{\odot}$ (Fig. 9, upper/left panel). As ϵ_{CII} is almost independent on the GMC model, in the rest of the discussion we will refer to the fiducial GMC case, i.e. model B.

4.1 [C II] line emission

In Fig. 10 we plot the [C II] luminosity for model B as a function of G_0 , and time, t , elapsed from the onset of the cloud illumination by a nearby starburst. The [C II] line has critical densities $n_{\text{crit}}^e \approx 50 \text{ cm}^{-3}$ and $n_{\text{crit}}^H \approx 3 \times 10^3 \text{ cm}^{-3}$ for collisions with electrons and neutral hydrogen atoms, respectively. During the PE process, the clump density always exceeds n_{crit}^H (see Fig. 2), while the ICM density is sub-critical. Thus, ICM largely dominates [C II] emission over the clumps.

For $t < t_{\text{pe}}$, the [C II] emission decreases with metallicity for strong radiation fields ($\log G_0 > 2$). As already mentioned, in these conditions FUV photons largely ionize GMCs; the free electrons then dominate the [C II] excitation. However, as the ICM density exceeds the electron critical density the [C II] luminosity is quenched.

At fixed metallicity, instead, [C II] increases with G_0 . The relation almost flattens for $\log G_0 \geq 3$ as the PDR temperature exceeds the [C II] $158 \mu\text{m}$ transition excitation temperature (92 K; see Fig. 5). At that point a further temperature increase does not appreciably change the [C II] line emission (e.g. Kaufman et al. 1999). The flattening trend

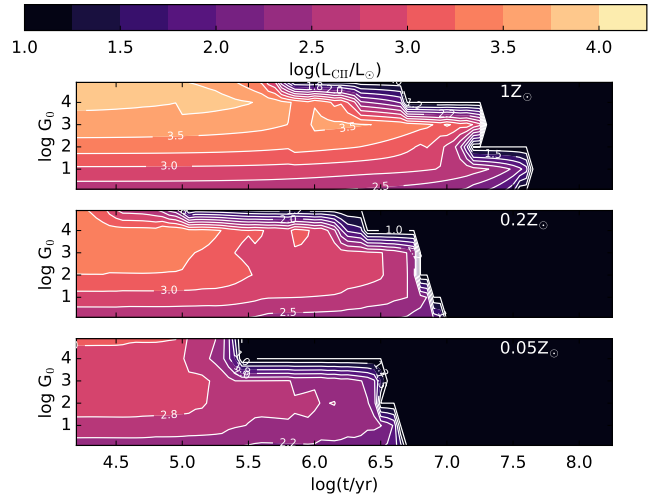


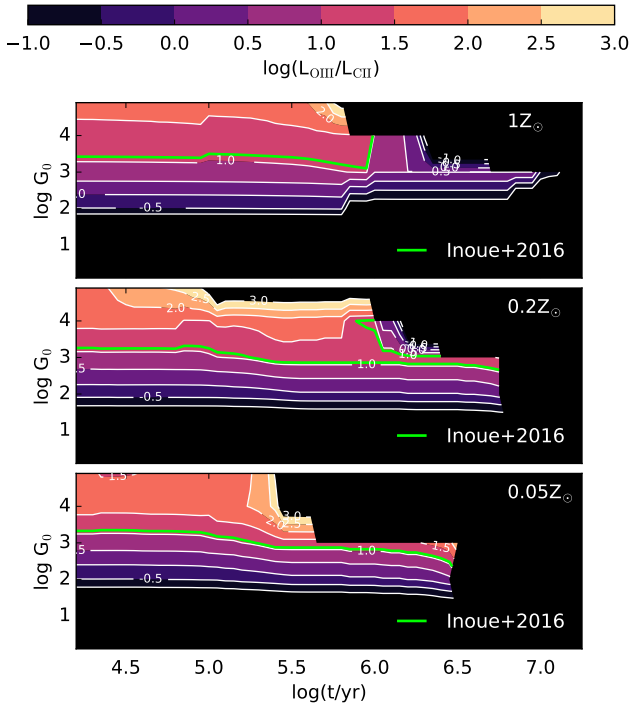
Figure 10. [C II] luminosity evolution as a function of G_0 for GMC model B and for different metallicities ($Z = Z_{\odot}$ upper panels, $Z = 0.2 Z_{\odot}$ middle, and $Z = 0.05 Z_{\odot}$ lower). Black regions denote $L_{\text{CII}} < 10 L_{\odot}$.

is enhanced at $Z = 0.05 Z_{\odot}$ because T_{PDR} is overall higher than for $Z = Z_{\odot}$.

Note that a GMC exposed to a low G_0 , albeit fainter in [C II] emission, survives for a longer time. Thus, L_{CII} reaches a maximum at progressively later times as G_0 is decreased. This behavior is a characteristic imprint of the PE process, and hence is generally valid for all FIR lines (see the next Section regarding the [O III]). The effect of PE on the FIR line luminosity in low-metallicity GMCs can be also appre-

Table 2. The coefficients of the polynomial fit for the [C II] and [O III] specific luminosities at $t = 10^5$ yr, as expressed in Equation 12

Coefficients	[C II] specific luminosity			[O III] specific luminosity		
	$Z = Z_{\odot}$	$Z = 0.2Z_{\odot}$	$Z = 0.05Z_{\odot}$	$Z = Z_{\odot}$	$Z = 0.2Z_{\odot}$	$Z = 0.05Z_{\odot}$
α	-2.424	-2.476	-2.652	-2.616	-9.079	-9.661
β	0.375	0.505	0.314	-9.298	1.088	1.075
γ	0.022	-0.102	-0.003	5.233	0.922	0.929
δ	-0.009	0.007	-0.015	-0.694	-0.168	-0.168

**Figure 11.** Time evolution of the $L_{\text{OIII}}/L_{\text{CII}}$ ratio as a function of G_0 for different metallicities ($Z = Z_{\odot}$ upper panel, $Z = 0.2 Z_{\odot}$ middle, and $Z = 0.05 Z_{\odot}$ lower) for cloud model B. Black regions denote the parameter space where the ratio is either non-defined or $\log(L_{\text{OIII}}/L_{\text{CII}}) < -1$. The green level represents the lower limit on [O III]/[C II] for the Ly α emitting galaxy SXDF-NB1006-2 located at $z = 7.2$ (Inoue et al. 2016).

ciated from Fig. 10: the L_{CII} after at 10 Myr drops dramatically with Z as a result of PE.

A simple polynomial fit describes the specific [C II] luminosity at $t = 10^5$ yr as a function of G_0 :

$$\log\left(\frac{\epsilon_{\text{CII}}}{L_{\odot} M_{\odot}^{-1}}\right) = \alpha + \beta \log G_0 + \gamma (\log G_0)^2 + \delta (\log G_0)^3 \quad (12)$$

The coefficients are listed in Table 2. These results are valid up to t_{pe} (see Table ??) with a precision better than 5% in the range $\log G_0 = 0 - 4$.

4.2 [O III] line emission

In this Section we extend our analysis to the [O III] $^3P_1 \rightarrow ^3P_0$ line at $88 \mu\text{m}$, one of the most prominent tracers of dense ionized gas at the transition with the photodissociation regions (e.g Cormier et al. 2012). The [O III] line predominantly arises from the cloud external ionized layer, as the O^+ ionization potential is $IP_{\text{O}^+} = 35.5 > 13.6$ eV. Note that the critical density for collisions with free electrons is $n_{crit}^e \approx 510 \text{ cm}^{-3} \approx \langle n_{\text{ICM}} \rangle$ of the model B.

In a recent paper Inoue et al. (2014) noted that ALMA capabilities might allow a combined study of the cold/neutral gas via the [C II] line, and of the warm/ionized component using the [O III] $88 \mu\text{m}$ transition well within the EoR. As a matter of fact, the [O III] line is often reported to be stronger than [C II] in low-metallicity nearby dwarf galaxies (Cormier et al. 2012; Madden et al. 2013; Cormier et al. 2015). As a result, the [O III]/[C II] may become increasingly higher at high redshift where galaxies have, on average, a lower metal content. In addition, the [O III] $88 \mu\text{m}$ line is not affected by dust extinction as it is in the case for other rest-frame UV/optical lines commonly used to probe H II regions. Cormier et al. (2012) showed that in local low-metallicity galaxies up to 60% of the total [O III] $88 \mu\text{m}$ emission originates from dense H II regions close to the starbursts. As we only deal with GMCs, our results on the [O III] luminosity must be considered as solid lower bound to the luminosity of this line.

The time evolution of the [O III]/[C II] ratio is plotted in Fig. 11. As expected, the [O III]/[C II] is correlated with G_0 . For $\log G_0 \leq 3.5$ the ratio is almost independent of metallicity, while for $\log G_0 > 3.5$ the [O III]/[C II] increases with decreasing metallicity. If the field is weak the ionized layer is anyway thin and metallicity variations do not alter the ratio. However, for strong fields and lower metal/dust content the ionized layer becomes thick and boosts [O III] line emission. However, due to the shorter photoevaporation time, at low-metallicities the maximum [O III]/[C II] ratio ([O III]/[C II] = 1000 for $\log G_0 > 4$) can be sustained for shorter times ($t \approx 10^6$ yr at $Z = 0.2 Z_{\odot}$ vs. $10^{5.4} \leq t \leq 10^{5.6}$ yr at $Z = 0.05 Z_{\odot}$).

Our time-dependent calculation shows that in unevolved ($Z \leq 0.2 Z_{\odot}$) and powerful ($\log G_0 \geq 3$) starbursts, it is possible to achieve [O III]/[C II] > 10 lasting 3 – 5 Myr. This is in line with the recent findings by Inoue et al. (2016) for the $z = 7.2$ Ly α emitting galaxy SXDF-NB1006-2. In Fig. 11 we plot the lower limit on SXDF-NB1006-2 ([O III]/[C II] $_{\text{NB1006}} > 12$) for the three metallicities considered in this work. From SED fitting Inoue et al. (2016) also find that $Z = 0.1 Z_{\odot}$ is the most probable value for SXDF-

NB1006-2, though $0.05 Z_{\odot} < Z < 1 Z_{\odot}$ cannot be rejected at a confidence level $> 3\sigma$.

Finally, as in the case of the [C II] line, in Table 2 we report the coefficients of the best polynomial fit for $\log(\epsilon_{\text{O III}}/L_{\odot}M_{\odot}^{-1})$ as expressed in Eq. 12, with a precision better than 5% in the range $\log G_0 = 1 - 4$.

5 SUMMARY AND CONCLUSIONS

We have studied the effects of photoevaporation of GMCs irradiated by an external UV radiation field. Our model allows to compute the evolution of the GMC density field and calculate the far-infrared (FIR) line luminosity emitted by the cloud during this process. The model includes: (i) three different GMC models, with properties derived from a combination of observational and simulated results, (ii) their time evolution during the photoevaporation process.

By exploring UV field intensities (in Habing units) in the range $G_0 = 1 - 10^5$ and gas metallicities $Z = 1, 0.2, 0.05 Z_{\odot}$, we find that the fiducial GMC (model B in Table 1) is completely photoevaporated in a timescale $t_{pe} \leq 30$ Myr. This timescale is comparable to that deduced for destruction due to expanding H II regions around newborn stars inside GMCs (Williams & McKee 1997; Krumholz et al. 2006).

The PE timescale is a decreasing function of metallicity, and it goes from 30 Myr at $Z = Z_{\odot}$, to 1 Myr at $Z = 0.05 Z_{\odot}$ for the fiducial cloud. This is because the increased penetration of FUV leads to thicker and hotter PDRs leading to a faster photoevaporation. Due to similar physical reasons, at fixed metallicity, t_{pe} decreases for higher FUV fluxes. The presence of ionizing EUV photons becomes important for low metallicities ($Z \leq 0.2 Z_{\odot}$) and strong ($\log G_0 > 4$) radiation fields, when the column density of the ionized layer becomes comparable to the total GMC one.

We compute the evolution of [C II], and [O III] line luminosity during the PE process. We show that the [C II] emission per unit mass ($\epsilon_{\text{C II}}$) for the three GMC models is independent of the internal GMC properties (i.e. the cloud model) and is a function of G_0 only, modulo a scaling factor $\propto t_{pe}$ entering the time evolution. It is then possible to specialize our results to the fiducial case (model B) only.

FIR line luminosities depend on: (a) time, t , elapsed from onset of irradiation; (b) metallicity, Z , of the GMC; (c) UV field intensity, G_0 . Albeit the interplay of these parameters is complex, a well-defined general trend emerges. Stronger UV fluxes produce higher [C II], and [O III] luminosities, however lasting for progressively shorter times (i.e. t_{pe} decreases along this sequence). More specifically, we find that:

1. For $Z = Z_{\odot}$ [C II] emission peaks at $t \lesssim 1$ Myr and $\log G_0 \geq 3$; the peak amplitude decreases towards lower metallicities. At fixed Z the [C II] correlates with G_0 , even though such trend is relatively mild and tends to flatten, particularly at very low metallicity ($Z = 0.05 Z_{\odot}$). Note that a GMC exposed to a low G_0 is less luminous but its emission phase can last longer.

2. Low metallicities ($Z \leq 0.2 Z_{\odot}$) and high UV fluxes ($\log G_0 \approx 4$) maximize the [O III]/[C II] ratio, pushing it to values up to ≈ 1000 . However, due to the shorter t_{pe} , for

very low metallicity such intense [O III] emission phase can be sustained only for $10^{5.4} \leq t \leq 10^{5.6}$ yr at $Z = 0.05 Z_{\odot}$.

3. The above results are consistent with recent observations of a LAE at $z \approx 7.2$ (Inoue et al. 2016), showing a [O III]/[C II] ratio > 12 and $Z \approx 0.1 Z_{\odot}$. Under these conditions we find that gas metallicities $Z \leq 0.2 Z_{\odot}$ allow to sustain [C II]/[O III] = 12 for $\approx 10^{6.5} - 10^{6.7}$ yr.

Although physically solid, our model has some caveats. As star formation within the GMC is not considered, the effects of internal radiation sources is not accounted for. Given that the star formation efficiency per free-fall time, ϵ_{eff} , varies considerably in GMCs (e.g. Semenov et al. 2015, $\epsilon_{eff} = 0.1 - 10\%$), the estimate of the actual number of OB stars depends strongly on the local conditions of the GMC. Williams & McKee (1997) estimate that for clouds of mass $10^5 M_{\odot}$, about half are expected to contain at least one OB star. By the way note that if an OB star forms in the GMC, the result of its ignition is to provide high UV fluxes to the cloud⁸. The photoevaporation timescales for a GMC destroyed by internal OB association that form blister H II regions is $t_{pe} \approx 30 - 40$ Myr (Williams & McKee 1997), which is comparable to that found with our modeling at solar metallicity.

To conclude, we have pointed out that photoevaporation of GMCs dramatically affects their survival and FIR emission properties in a complex way. This has to be kept in mind when interpreting the FIR line data from high- z galaxies, which are metal poor and characterized by hard interstellar radiation fields, all conditions leading to fast photoevaporation. As already pointed out in Vallini et al. (2015) photoevaporation feedback might be responsible for the observed spatial displacement of FIR line-emitting sites with respect to the UV continuum position. In the central regions, in fact, GMC might be evaporated by the powerful radiation field, with the result that FIR lines are suppressed in the vicinity of the star-forming region. The impact of such effects on galactic scales will be explored in a forthcoming study.

ACKNOWLEDGMENTS

We thank the anonymous referees for their thorough and constructive comments that have greatly improved the paper. We are indebted to D. Cormier, A. Citro, E. Sobacchi, and F. Pacucci for useful comments. We thank all the participants of *The Cold Universe* program held in 2016 at the KITP, UC Santa Barbara, for valuable comments and discussions during the workshop. This research was supported in part by the National Science Foundation under Grant No. NSF PHY11-25915.

REFERENCES

Bayet E., Williams D. A., Hartquist T. W., Viti S., 2011, *MNRAS*, **414**, 1583
 Bertoldi F., 1989, *ApJ*, **346**, 735

⁸ The Habing flux provided by an O star at ≈ 0.1 pc from its surface is $\log G_0 \approx 6$ (Hollenbach & Tielens 1999)

- Bertoldi F., McKee C. F., 1990, *ApJ*, **354**, 529
- Bisbas T. G., Bell T. A., Viti S., Yates J., Barlow M. J., 2012, *MNRAS*, **427**, 2100
- Bisbas T. G., Papadopoulos P. P., Viti S., 2015, *ApJ*, **803**, 37
- Bonnell I. A., Dobbs C. L., Robitaille T. P., Pringle J. E., 2006, *MNRAS*, **365**, 37
- Bothwell M. S., et al., 2016, preprint, ([arXiv:1612.04380](https://arxiv.org/abs/1612.04380))
- Cardelli J. A., Meyer D. M., Jura M., Savage B. D., 1996, *ApJ*, **467**, 334
- Carilli C. L., Walter F., 2013, *ARA&A*, **51**, 105
- Cartledge S. I. B., Lauroesch J. T., Meyer D. M., Sofia U. J., 2004, *ApJ*, **613**, 1037
- Cormier D., et al., 2012, *A&A*, **548**, A20
- Cormier D., et al., 2015, *A&A*, **578**, A53
- Dale J. E., Ngoumou J., Ercolano B., Bonnell I. A., 2013, *MNRAS*, **436**, 3430
- Dale J. E., Ngoumou J., Ercolano B., Bonnell I. A., 2014, *MNRAS*, **442**, 694
- Elmegreen B. G., Scalo J., 2004, *ARA&A*, **42**, 211
- Falgarone E., Phillips T. G., 1990, *ApJ*, **359**, 344
- Federrath C., Klessen R. S., 2012, *ApJ*, **761**, 156
- Federrath C., Klessen R. S., 2013, *ApJ*, **763**, 51
- Ferland G. J., et al., 2013, *Rev. Mexicana Astron. Astrofis.*, **49**, 137
- Gallerani S., Pallottini A., Feruglio C., Ferrara A., Maiolino R., Vallini L., Riechers D. A., 2016, preprint, ([arXiv:1604.05714](https://arxiv.org/abs/1604.05714))
- Goicoechea J. R., et al., 2015, *ApJ*, **812**, 75
- Goldsmith P. F., Heyer M., Narayanan G., Snell R., Li D., Brunt C., 2008, *ApJ*, **680**, 428
- Gong Y., Cooray A., Silva M., Santos M. G., Bock J., Bradford C. M., Zemcov M., 2012, *ApJ*, **745**, 49
- Goodman A. A., Pineda J. E., Schnee S. L., 2009, *ApJ*, **692**, 91
- Gorti U., Hollenbach D., 2002, *ApJ*, **573**, 215
- Habing H. J., 1968, *Bull. Astron. Inst. Netherlands*, **19**, 421
- Hennebelle P., Chabrier G., 2011, *ApJ*, **743**, L29
- Hennebelle P., Chabrier G., 2013, *ApJ*, **770**, 150
- Hollenbach D. J., Tielens A. G. G. M., 1999, *Reviews of Modern Physics*, **71**, 173
- Indriolo N., McCall B. J., 2013, *Chem. Soc. Rev.*, **42**, 7763
- Indriolo N., Geballe T. R., Oka T., McCall B. J., 2007, *ApJ*, **671**, 1736
- Inoue A. K., Shimizu I., Tamura Y., Matsuo H., Okamoto T., Yoshida N., 2014, *ApJ*, **780**, L18
- Inoue A. K., et al., 2016, preprint, ([arXiv:1606.04989](https://arxiv.org/abs/1606.04989))
- Kainulainen J., Lada C. J., Rathborne J. M., Alves J. F., 2009, *A&A*, **497**, 399
- Kaufman M. J., Wolfire M. G., Hollenbach D. J., Luhman M. L., 1999, *ApJ*, **527**, 795
- Kim W.-T., Ostriker E. C., Stone J. M., 2003, *ApJ*, **599**, 1157
- Kim J.-G., Kim W.-T., Ostriker E. C., 2016, *ApJ*, **819**, 137
- Knudsen K. K., Richard J., Kneib J.-P., Jauzac M., Clement B., Drouart G., Egami E., Lindroos L., 2016, preprint, ([arXiv:1603.02277](https://arxiv.org/abs/1603.02277))
- Körtgen B., Seifried D., Banerjee R., Vázquez-Semadeni E., Zamora-Avilés M., 2016, *MNRAS*, **459**, 3460
- Krumholz M. R., McKee C. F., 2005, *ApJ*, **630**, 250
- Krumholz M. R., Matzner C. D., McKee C. F., 2006, *ApJ*, **653**, 361
- Leitherer C., et al., 1999, *APJS*, **123**, 3
- Lejeune T., Cuisinier F., Buser R., 1997, *A&AS*, **125**
- Lombardi M., Alves J., Lada C. J., 2015, *A&A*, **576**, L1
- Mac Low M.-M., Klessen R. S., 2004, *Reviews of Modern Physics*, **76**, 125
- Madden S. C., et al., 2013, *PASP*, **125**, 600
- Maiolino R., et al., 2015, *ArXiv e-prints:1502.06634*
- McKee C. F., Ostriker E. C., 2007, *ARA&A*, **45**, 565
- Meijerink R., Spaans M., Loenen A. F., van der Werf P. P., 2011, *A&A*, **525**, A119
- Meixner M., Tielens A. G. G. M., 1993, *ApJ*, **405**, 216
- Molina F. Z., Glover S. C. O., Federrath C., Klessen R. S., 2012, *MNRAS*, **423**, 2680
- Nagamine K., Wolfe A. M., Hernquist L., 2006, *ApJ*, **647**, 60
- Nakamura F., Li Z.-Y., 2014, *ApJ*, **783**, 115
- Norman C., Silk J., 1980, *ApJ*, **238**, 158
- Olsen K. P., Greve T. R., Narayanan D., Thompson R., Toft S., Brinch C., 2015, *ApJ*, **814**, 76
- Osterbrock D. E., Tran H. D., Veilleux S., 1992, *ApJ*, **389**, 305
- Padoan P., Nordlund Å., 2011, *ApJ*, **730**, 40
- Padoan P., Federrath C., Chabrier G., Evans II N. J., Johnstone D., Jørgensen J. K., McKee C. F., Nordlund Å., 2014, *Protostars and Planets VI*, pp 77–100
- Pallottini A., Gallerani S., Ferrara A., Yue B., Vallini L., Maiolino R., Feruglio C., 2015, *MNRAS*, **453**, 1898
- Pallottini A., Ferrara A., Gallerani S., Vallini L., Maiolino R., Salvadori S., 2017, *MNRAS*, **465**, 2540
- Papadopoulos P. P., Thi W.-F., Miniati F., Viti S., 2011, *MNRAS*, **414**, 1705
- Rubin R. H., Simpson J. P., Haas M. R., Erickson E. F., 1991, *ApJ*, **374**, 564
- Rubin R. H., Dufour R. J., Walter D. K., 1993, *ApJ*, **413**, 242
- Schaller G., Schaerer D., Meynet G., Maeder A., 1992, *A&AS*, **96**, 269
- Schmutz W., Leitherer C., Gruenwald R., 1992, *PASP*, **104**, 1164
- Schneider N., et al., 2015, preprint, ([arXiv:1509.01082](https://arxiv.org/abs/1509.01082))
- Semenov V. A., Kravtsov A. V., Gnedin N. Y., 2015, preprint, ([arXiv:1512.03101](https://arxiv.org/abs/1512.03101))
- Stutz A. M., Kainulainen J., 2015, *A&A*, **577**, L6
- Tasker E. J., Tan J. C., 2009, *ApJ*, **700**, 358
- Vallini L., Gallerani S., Ferrara A., Baek S., 2013, *MNRAS*, **433**, 1567
- Vallini L., Gallerani S., Ferrara A., Pallottini A., Yue B., 2015, *ApJ*, **813**, 36
- Vázquez-Semadeni E., 1994, *ApJ*, **423**, 681
- Vázquez-Semadeni E., Kim J., Ballesteros-Paredes J., 2005, *ApJ*, **630**, L49
- Vázquez-Semadeni E., Colín P., Gómez G. C., Ballesteros-Paredes J., Watson A. W., 2010, *ApJ*, **715**, 1302
- Visser R., et al., 2012, *A&A*, **537**, A55
- Wada K., 2008, *ApJ*, **675**, 188
- Wada K., Norman C. A., 2001, *ApJ*, **547**, 172
- Walch S., Naab T., 2015, *MNRAS*, **451**, 2757
- Williams J. P., McKee C. F., 1997, *ApJ*, **476**, 166
- Williams J. P., Blitz L., Stark A. A., 1995, *ApJ*, **451**, 252
- Wolfire M. G., McKee C. F., Hollenbach D., Tielens A. G. G. M., 2003, *ApJ*, **587**, 278
- Zhang Z.-Y., Papadopoulos P. P., Ivison R. J., Galametz M., Smith M. W. L., Xilouris E. M., 2016, *Royal Society Open Science*, **3**, 160025
- da Cunha E., et al., 2013, *ApJ*, **766**, 13

APPENDIX A: PENETRATION OF EUV AND FUV PHOTONS

When the GMC is embedded in an H II region, the ICM is exposed to both EUV and FUV photons, while the internal clumps see only the attenuated FUV radiation. Lyman continuum photons penetrate a gas slab of density n , and surface area S , up to a depth d given by:

$$d = \frac{\dot{N}_{ion}}{S n^2 \alpha_{rec}} \approx \frac{F_{ion}}{(h\nu) n^2 \alpha_{rec}}, \quad (\text{A1})$$

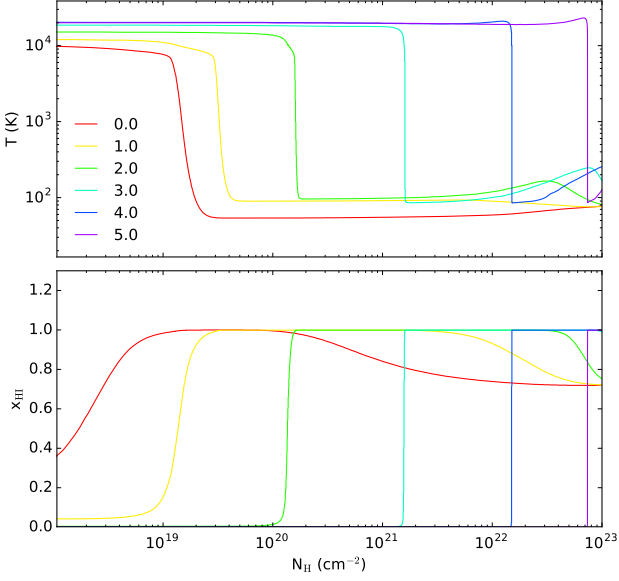


Figure A1. Temperature and x_{HI} profiles obtained with CLOUDY when considering a gas slab characterized by $n = 100 \text{ cm}^{-3}$ and illuminated by SED resulting from continuous star formation at 1 Myr. The lines are color coded according to $\log G_0$ at the gas slab surface.

where $\alpha_{\text{rec}} = 3 \times 10^{-13} \text{ cm}^3 \text{ s}^{-1}$ is the hydrogen recombination rate coefficient, \dot{N}_{ion} the number of ionizing photons per second, $F_{\text{ion}} = L_{\text{ion}}/S$ is the ionizing photon flux, L_{ion} the ionizing luminosity ($L_{\text{ion}} = \int L_{\lambda} d\lambda$ for $\lambda < 912 \text{ \AA}$), and $h\nu \approx 2.1 \times 10^{-11} \text{ erg}$ is the energy of Lyman limit photons. For the SED used in the present work (see Fig. 3), the ionizing luminosity is $L_{\text{ion}} \approx 0.3 L_{\text{Habing}}$ at 1 Myr. Hence, we can give an estimate of the column penetrated by EUV photons in term of the Habing flux as follows:

$$\begin{aligned} N_{\text{HII}} &= nd = \frac{F_{\text{ion}}}{h\nu} \frac{1}{n\alpha_{\text{rec}}} \approx \\ &\approx 7 \times 10^{17} \frac{n}{100 \text{ cm}^{-3}} \frac{G_0}{\text{erg s}^{-1} \text{ cm}^{-2}} \text{ cm}^{-2}. \end{aligned} \quad (\text{A2})$$

For example, for $G_0 = 10^4 - 10^5$ (typical of the PDRs near OB associations) and $n = 100 \text{ cm}^{-3}$ the eq. yields $N_{\text{HII}} = 7 \times 10^{21} - 7 \times 10^{22} \text{ cm}^{-2}$. In Fig. A1 we show the temperature and neutral fraction ($x_{\text{HI}} = n_{\text{HI}}/n$) profiles as a function of N_H . The profiles are obtained with CLOUDY simulations that consider the whole SED (EUV+FUV) impinging on a gas slab with $n = 100 \text{ cm}^{-3}$ (typical of ICM) and $Z = 0.05 Z_{\odot}$. The profiles are color-coded as a function of the Habing flux at the slab surface.

The full CLOUDY calculation returns ionized columns $N_{\text{HII}} \approx 1.5 - 7 \times 10^{22} \text{ cm}^{-2}$ for $G_0 = 10^4 - 10^5$, i.e. in good agreement with the estimate that can be obtained from Eq.s A1 and A2 for a gas slab of pure hydrogen. The HII columns for a gas slab with $Z = 1 Z_{\odot}$ are $N_{\text{HII}} \approx 4 \times 10^{21} \text{ cm}^{-2}$ for $G_0 = 10^4$ and $N_{\text{HII}} \approx 7 \times 10^{21} \text{ cm}^{-2}$ for $G_0 = 10^5$.

Note that above such column density, any H-ionizing photons are then absorbed in a thin ($N_H \approx 10^{19} \text{ cm}^{-2}$ or $\Delta A_V \approx 10^{-2}$) transition zone in which the ionization structure changes from being almost fully ionized ($x_e \approx 1$) to

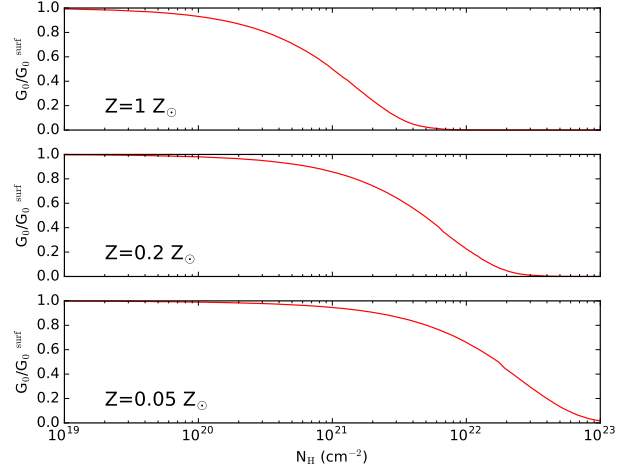


Figure A2. Profile of the G_0 attenuation as resulting from CLOUDY simulations considering a gas slab characterized by $n = 100 \text{ cm}^{-3}$ and $Z = 1, 0.2, 0.05 Z_{\odot}$ from top to bottom.

being almost fully neutral ($x_e \approx 10^{-4}$) (Hollenbach & Tielens 1999).

In Fig. A2 we plot the attenuation of the Habing flux (G_0/G_0^{surf}) through the gas slab as a function of the metallicity. As we assume a dust-to-gas ratio that scales linearly with Z , at lower Z corresponds a lower G_0 attenuation. These profiles are adopted to compute the average Habing field impinging the clump surfaces $\langle G_0^{\text{clumps}} \rangle = \langle f_{\text{att}} \rangle G_0^{\text{surf}}$, with:

$$\langle f_{\text{att}} \rangle = G_0 (\langle N_{\text{H}}^{\text{ICM-clumps}} \rangle) / G_0^{\text{surf}}, \quad (\text{A3})$$

where $\langle N_{\text{H}}^{\text{ICM-clumps}} \rangle$ is the mean column of gas in the ICM between the GMC and the clump surfaces. $\langle N_{\text{H}}^{\text{ICM-clumps}} \rangle = n_{\text{ICM}}(l)$ is calculated by sampling the location (l) of the clumps in the GMC via a monte-carlo acceptance-rejection method by assuming (i) a uniform clump distribution, and (ii) the GMC to be spherical. The mean radius is $\langle l \rangle = 0.25 r_{\text{GMC}}$.

APPENDIX B: PHOTOEVAPORATION MODEL

Clumps are assumed to be dense, small spheres of initial radius r_{cl}^0 , and initial density n_{cl}^0 , supported by thermal, turbulent, and magnetic pressures. The magnetic field B scales with a constant power of the density so that the magnetic pressure is $P_B \propto n^{\gamma}$. The ratios of turbulent, and magnetic pressures, over the thermal pressure are indicated with $\alpha \equiv P_{\text{turb}}/P_T$ and $\beta \equiv P_B/P_T$. The fiducial values in Gorti & Hollenbach (2002), kept fixed in our work, are $\alpha = \beta = 1$ and $\gamma = 4/3$.

B1 Evolution of shock-compressed clumps

Let $r_{\text{cl}}(0) = r_{\text{cl}}^0 - \delta_0$, where $\delta_0 = N_0/n_{\text{cl}}^0$ is the initial thickness of PDR shell on the surface of the clump. In the case of shock-compressed clumps, Gorti & Hollenbach

(2002) demonstrated (cfr. eq.s from B1 to B17 in their paper) that the shock compression shrinks the clump in a time $t_s \simeq r_{cl}(0)/c_{PDR}$ to a radius r_s . The clump mass at $t = t_s$ is:

$$m_c(t_s) = m_{cl}(0) - 8\pi m_H N_0 r_{cl}(0)^2 \frac{v_b}{2c_{PDR}} \quad (\text{B1})$$

where $v_b \approx 0.7c_{PDR}$ is the average velocity with which the radius decreases. After being compressed by the shock, the clump radius and mass evolve as:

$$r_{cl}(t > t_s) = \left(\left[\left[\frac{r_s}{r_{cl}(0)} \right]^{2-1/\gamma} \right] - \frac{2\gamma-1}{3\gamma-1} \frac{6\nu\eta_0}{(\eta_0-1)^2} \times \left[\frac{\beta(\eta_0-1)}{2(2\nu^2+\alpha)} \right]^{1/\gamma} \left[\frac{t}{t_c} - \frac{(\eta_0-1)}{\eta_0\nu} \right] \right)^{\gamma/(2\gamma-1)} \quad (\text{B2})$$

and

$$m_{cl}(t > t_s) = m_{cl}(0) \left[\frac{2(2\nu^2+\alpha)}{\beta(\eta_0-1)^2} \right]^{1/\gamma} \left[\frac{r_{cl}(t)}{r_{cl}(0)} \right]^{3-1/\gamma}. \quad (\text{B3})$$

The photoevaporation timescale, obtained by setting the clump radius to zero, is

$$t_{pe} = t_c \left[\left[\frac{r_s}{r_{cl}(0)} \right]^{2-1/\gamma} \left(\frac{3\gamma-1}{2\gamma-1} \right) \times \frac{(\eta_0-1)^2}{6\nu\eta_0} \left[\frac{2(2\nu^2+\alpha)}{\beta(\eta_0-1)} \right]^{1/\gamma} + \frac{\eta_0-1}{\eta_0\nu} \right] \quad (\text{B4})$$

B2 Evolution of clumps with initial expansion

Assuming that the clumps expands in the vacuum (cfr. eq.s from C1 to C7 in [Gorti & Hollenbach 2002](#)) at their sound speed c_c until the pressure drops to that in the heated outer layer, it is possible to demonstrate that the expansion time is:

$$t_e = t_c \left(1 - \frac{1}{\eta_0} \right) \left[\left[\frac{3\nu + \eta_0 - 1}{3\nu 2(2\nu^2 + \alpha)/(1 + \alpha)} \right]^{1/2} - 1 \right]. \quad (\text{B5})$$

The time evolution of the clump radius and mass at $t > t_e$ is:

$$r_{cl}(t > t_e) = r_{cl}(t_e) - \frac{3}{2} c_{PDR} \frac{1 + \alpha}{2\nu^2 + \alpha} (t - t_e), \quad (\text{B6})$$

and

$$m_{cl}(t > t_e) = m_{cl}^0 \frac{2(2\nu^2 + \alpha)}{\eta_0(1 + \alpha)} \left[\frac{r_{cl}(t)}{r_c^0} \right]^2. \quad (\text{B7})$$

The photoevaporation timescale is obtained by setting the clump radius to zero

$$t_{pe} = \left(\frac{2\nu^2 + \alpha}{1 + \alpha} \right) \frac{r_{cl}(0) + c_c t_e}{3c_{PDR}} + t_e \quad (\text{B8})$$

This paper has been typeset from a $\text{\TeX}/\text{\LaTeX}$ file prepared by the author.